



Published in final edited form as:

Nat Biotechnol. 2016 April ; 34(4): 414–418. doi:10.1038/nbt.3506.

## An injectable nanoparticle generator enhances delivery of cancer therapeutics

Rong Xu<sup>1,2,\*</sup>, Guodong Zhang<sup>1,\*</sup>, Junhua Mai<sup>1,\*</sup>, Xiaoyong Deng<sup>1,8,\*</sup>, Victor Segura-Ibarra<sup>1</sup>, Suhong Wu<sup>1</sup>, Jianliang Shen<sup>1</sup>, Haoran Liu<sup>1</sup>, Zhenhua Hu<sup>1</sup>, Lingxiao Chen<sup>1</sup>, Yi Huang<sup>1</sup>, Eugene Koay<sup>1,3</sup>, Yu Huang<sup>1,9</sup>, Jun Liu<sup>4</sup>, Joe E. Ensor<sup>5</sup>, Elvin Blanco<sup>1</sup>, Xuewu Liu<sup>1</sup>, Mauro Ferrari<sup>1,6,#</sup>, and Haifa Shen<sup>1,7,#</sup>

<sup>1</sup>Department of Nanomedicine, Houston Methodist Research Institute, Houston, Texas, USA

<sup>2</sup>Department of Pharmacology, School of Basic Medicine, Tongji Medical College, Huazhong University of Science and Technology, Wuhan, China

<sup>3</sup>Division of Radiation Oncology, The University of Texas M. D. Anderson Cancer Center, Houston, Texas, USA

<sup>4</sup>Department of Pathology and Laboratory Medicine, The University of Texas-Houston Medical School, Houston, Texas, USA

<sup>5</sup>Houston Methodist Cancer Center, Houston, Texas 77030, USA

<sup>6</sup>Department of Medicine, Weill Cornell Medical College, New York, New York, USA

<sup>7</sup>Department of Cell and Developmental Biology, Weill Cornell Medical College, New York, New York, USA

### Abstract

The efficacy of cancer drugs is often limited because only a small fraction of the administered dose accumulates in tumors. Here we report an injectable nanoparticle generator (iNPG) that overcomes multiple biological barriers to cancer drug delivery. The iNPG is a discoidal micrometer-sized particle that can be loaded with chemotherapeutics. We conjugate doxorubicin to poly(L-glutamic acid) via a pH-sensitive cleavable linker, and load the polymeric drug (pDox) into iNPG to assemble iNPG-pDox. Once released from iNPG, pDox spontaneously forms nanometer-sized particles in aqueous solution. Intravenously injected iNPG-pDox accumulates at tumors due to natural tropism and enhanced vascular dynamics and releases pDox nanoparticles that are internalized by tumor cells. Intracellularly, pDox nanoparticles are transported to the perinuclear

<sup>#</sup>Correspondence should be addressed to: M.F. (mferrari@HoustonMethodist.org) & H.S. (hshen@HoustonMethodist.org).

<sup>8</sup>Current address: Institute of Nanochemistry and Nanobiology, Shanghai University, Shanghai, China

<sup>9</sup>Current address: Biomedical Engineering Department, University of South Dakota, Sioux Falls, South Dakota, USA

\*These authors contributed equally to this work.

### Author contributions

M. F. and H. S. developed the concept, and supervised experiments. H. S., E. B., and M. F. prepared the manuscript with assistance from R. X., G. Z., X. D., and J. M., X. L. and Y. H. fabricated porous silicon particles. G. Z. and Z. H. synthesized pDox. G. Z., V. S.-I., S. W., and J. L. characterized iNPG-pDox. R. X., J. M., X. D., Z. H., J. S., Y. H., H. L., L. C. and E. K. performed *in vivo* biological analyses. J. E. E. performed biostatistical analysis.

### Competing financial interests

All authors declare no conflict of interest.

region and cleaved into Dox, thereby avoiding excretion by drug efflux pumps. Compared to its individual components or current therapeutic formulations, iNPG-pDox shows enhanced efficacy in MDA-MB-231 and 4T1 mouse models of metastatic breast cancer, including functional cures in 40–50% of treated mice.

A series of biological barriers hinders the accumulation of drugs in tumors<sup>1–3</sup>, reducing the efficacy of conventional and nanoparticle-based chemotherapeutics, especially in the treatment of metastatic disease<sup>4, 5</sup>. Among these barriers are drug distribution to non-tumor tissues<sup>6</sup>, hemorheological flow limitations and endothelial association/extravasation<sup>7</sup>, impaired delivery across tumor cell membranes and tissue<sup>8</sup> and multidrug resistance<sup>9</sup>. Multifunctional nanoparticles have been developed to surmount these barriers<sup>10</sup> (e.g., addition of moieties for active tumor targeting and pH-sensitive release), but they have shown limited success, and none has been adopted in the clinic. An effective solution will require a design that addresses all barriers successively, demonstrating substantial tropism to tumors, association with and extravasation across tumor-associated vascular endothelium, cellular internalization, vesicular transport to perinuclear regions, endosomal escape, and avoidance of multidrug resistance (MDR) efflux pumps. Here we describe an iNPG that sequentially negotiates these tasks. iNPG-pDox consists of nanoporous silicon particles<sup>11</sup> packaged with pDox that self-assembles into nanoparticles (Fig. 1a). Once iNPG-pDox has localized to tumor tissues due to natural tropism and favorable vascular dynamics, pDox molecules assemble into nanoparticles and are released intratumorally in a sustained fashion. Upon internalization in tumor cells, pDox nanoparticles undergo trafficking to perinuclear regions of the cell. There, a pH-sensitive linker<sup>12</sup> connecting the polymer to Dox is cleaved in the acidic environment of the endosomes<sup>13,14</sup>, yielding high intracellular concentrations of activated Dox in a cellular domain beyond the reach of cell-surface drug efflux pumps.

pDox was synthesized by covalently conjugating Dox to the glutamic acid side chains of poly(L-glutamic acid) via a pH-sensitive hydrazone linker (Supplementary Fig. 1a), and successful conjugation was confirmed by <sup>1</sup>H-NMR (Supplementary Fig. 1b). Physico-chemical parameters of the construct are summarized in Supplementary Table 1. pDox molecules were loaded into the 40–80 nm-sized pores of discoidal silicon-based carrier particles measuring 2.5 μm in diameter and 700 nm in thickness (Supplementary Fig. 2), with geometry and dimensions previously shown to optimize the concentration of particles in metastases, including lung and liver lesions<sup>15–17</sup>. Confocal microscopy confirmed pDox loading in to nanopores of the silicon-carrier, with pDox accounting for 25% of the total weight of iNPG-pDox (Supplementary Table 1). Upon loading, pDox distributed homogeneously throughout the nanopores, with intense drug-associated fluorescence (red) found co-localized (orange) with carrier-associated fluorescence (gray), which in turn spanned all levels of the construct from basal to top planes (Fig. 1b). Cross-sectional examination of iNPG-pDox with confocal microscopy, with specific emphasis on the region of the particles consisting of pore openings, visualized the release of pDox nanoparticles (red) from the silicon carrier construct (Fig. 1c). The size range of nanoparticles generated and released at physiological pH, as visualized by confocal microscopy, measured via AFM and cryogenic TEM (Fig. 1d and 1e), and corroborated by dynamic light scattering (DLS), proved to be 30–80 nm. pDox nanoparticles of analogous size were detected at pH 6.6

(Supplementary Fig. 3a), indicating that pDox remained in nanoparticle form upon release under the slightly acidic (pH 6.6–7.0) conditions that are also found in tumor microenvironments<sup>18</sup>. The resulting size range of pDox nanoparticles suggests that pDox assembled into nanoparticles upon contact with aqueous environments, and particle size was influenced by the pore of the iNPG (Supplementary Fig. 3a–b).

The kinetics of assembly, as well as pH sensitive cleavage of Dox from pDox, resulted in sustained release of pDox from iNPG for up to two weeks at pH 7.4 (Fig. 1f). Moreover, Dox was effectively cleaved from pDox at pH 5.2, but not at pH 7.4 (Fig. 1g), with release of Dox occurring at faster rates in acidic environments. The size of the released particles at pH 5.2 was less than 25 nm (Supplementary Fig. 3c), suggesting that pH-dependent cleavage of the pDox construct overtook nanoparticle assembly.

Both free pDox and iNPG-pDox proved effective at killing human triple-negative breast cancer cell lines MDA-MB-231 and MDA-MB-468 *in vitro* (Supplementary Fig. 4a–b), with conjugation of Dox to the polymer not substantially reducing the cell-killing activity of the active drug, indicating effective cleavage of Dox from pDox inside cells. To determine whether pH-dependent drug release from pDox was critical for cell-killing activity, an amide-pDox that shared a similar chemical structure as pDox, but lacked a pH-sensitive hydrazone linker between poly(L-glutamic acid) and Dox was synthesized (Supplementary Fig. 4c). This polymeric drug had only a fraction of the cell killing activity of pDox on MDA-MB-231 and MDA-MB-468 cells (Supplementary Fig. 4d), suggesting that effective cleavage of Dox from the polymer was essential for maximal tumor cell killing and demonstrating the vital role of pH-dependent drug release for overall activity.

Uptake of pDox in MDA-MB-231 cells was effectively blocked by inhibitors of the clathrin- and caveolae-mediated pathways including dynasore, chlorpromazine and genistein, but not by various inhibitors of phagocytosis or macropinocytosis, indicating that clathrin- and caveolae-mediated pathways play important roles in tumor cell internalization of pDox (Supplementary Fig. 5a). Compared to free Dox, pDox NP demonstrated a delayed cellular entry (Supplementary Fig. 5b). Fluorescence from pDox co-localized with LysoTracker-positive subcellular organelles 1 hour after treatment and reached a high level at 8 hours, indicating vesicular internalization and transport in cancer cells. Based on structural properties and pH- dependent cleavage profiles, pDox disassembled into free Dox and poly-glutamic acid in the acidic environment of endosomes<sup>14</sup>, with released Dox entering the nucleus directly from perinuclear compartments

*In vivo*, iNPG-pDox showed an effective natural tropism and accumulation to sites of metastasis. Biodistribution assays of Dox, pDox NP, and iNPG-pDox carried out in murine models of metastatic MDA-MB-231 tumors showed that drug cleared rapidly from circulation, regardless of formulation (Fig. 2a). High Dox concentration in the heart was detected 1 hour after dosing with free Dox, with accumulation leading to severe damage to cardiac myofibers (Supplementary Fig. 6), similar to clinical observations of severe cardiomyopathy in patients that imposes a maximum lifetime dosage threshold<sup>19, 20</sup>. By contrast, pDox and iNPG-pDox were not present at high levels in the heart (Fig. 2a), and there was no evidence of structural cardiac damage in the iNPG-pDox treatment group

(Supplementary Fig. 6). Moreover, high Dox concentrations were detected in kidneys of mice treated with free Dox and pDox, but not iNPG-pDox (Fig. 2a). Rapid renal clearance was most likely the cause of quick drop off levels of drug in the liver and lung in the free Dox and pDox treatment groups. Although there was no significant difference in drug accumulation in these organs 1 hour post-dosing between free Dox and iNPG-pDox treatment groups, higher levels of iNPG-pDox were detected in the liver 1 day and 7 days later.

Consistent and prominent contrast in Dox accumulation profiles could be seen in tumor-bearing lungs. There was a seven- fold enhancement in iNPG-pDox over free Dox 1 day after dosing, with high levels maintained in this organ up to 7 days (Fig. 2a), likely due to the stability of iNPG in acidic microenvironments of tumor-bearing tissues. Silicon content analysis confirmed accumulation and sustained presence of iNPG in livers and tumor-bearing lungs, and that iNPG particles were cleared from circulation within 1 hour after intravenous administration (Supplementary Fig. 7a). Intraperitoneal administration of iNPG-pDox did not result in comparable drug levels in the lungs of tumor-bearing mice as those observed following an intravenous administration of the drug (Supplementary Fig. 7b). This observation further corroborated the notion that the innate tropism and tumor tissue accumulation depends on intravenous administration of iNPG-pDox. Moreover, tumor-free nude mice treated with the same dose of Dox, pDox NP, and iNPG-pDox displayed similar drug levels in the heart and liver as those in tumor- bearing mice, but the amount of drug in lungs in the disease-free scenario was only a fraction of that found in lungs of tumor-bearing mice at all 3 time points examined (Supplementary Fig. 8, Fig. 2a).

Following organ-specific accumulation, we evaluated intratumoral iNPG-pDox distribution in the lungs as well as pDox NP uptake by cells. Real-time intravital microscopy revealed fluorescent iNPG-pDox particles in tumor nodules (Supplementary Fig. 9a). Histological analysis of tumors in the lung demonstrated accumulation of iNPG-pDox particles in tissues collected 1 hour and 24 hours after administration (Fig. 2b), with co-localization of the silicon carrier constructs and red blood cells in tumor nodules indicative of particle attachment to tumor microvascular walls (Fig. 2c–d, Supplementary Fig. 9b–c). TEM analysis of tumor tissues collected at the 24 hour time point confirmed tight attachment of the silicon carrier construct to tumor microvessels (Fig. 2e). Flow cytometry analysis of disseminated single cells from post-treatment tumor-bearing lung tissues corroborated microvessel enrichment of iNPG-pDox, with CD31<sup>+</sup> endothelial cells associated with the highest percentage of Dox (Fig. 2f). A higher percentage of tumor cells than normal lung cells were Dox-positive at both 4 hours and 24 hours, indicating that released pDox nanoparticles had been effectively taken up by tumor cells. Notably, there were more Dox-positive tumor cells in the iNPG-pDox treatment group than in Doxil (liposome-encapsulated Dox) [AU:OK? ok] or free Dox groups (Fig 2f). Tissue sectioning 24 hours after administration showed cell apoptotic bodies in tumor tissues from mice treated with iNPG-pDox (Supplementary Fig. S10).

Mice bearing metastatic MDA-MB-231 tumors in the lung were used to validate the therapeutic efficacy of iNPG-pDox compared to equivalent amounts of clinical formulations of Dox (Fig. 3a–b). H&E staining of lung tissues from athymic nude mice sacrificed at the

end of drug treatments (week 7) revealed the presence of smaller and fewer tumor nodules in mice treated with Doxil or iNPG-pDox compared to PBS controls (Supplementary Fig. 11a), a difference reflected as well by Ki-67 staining for proliferating tumor cells (Supplementary Fig. 11b). Treatment with free Dox or pDox offered limited survival benefit compared to negative controls (Fig. 3). Mice treated with Doxil extended median survival by 37 days. Tumor growth stalled during the 6-week treatment period, but resumed as soon as treatment was discontinued. The most efficacious therapeutic effect was observed in mice undergoing iNPG-pDox treatment, with 80% of mice remaining alive after 20 weeks when all mice in the control groups had succumbed to disease, and 50% achieving long-term survival (Fig. 3b).

An additional efficacy examination was performed in BALB/c mice bearing 4T1 tumors. The primary 4T1 tumors metastasized to the liver and lung in this model. Histological analysis corroborated iNPG-pDox accumulation in lung tumor nodules (Supplementary Fig. 12). PBS and iNPG vehicle control mice began to expire from lung metastases in week 6, with all mice succumbing to the disease by week 9 (Supplementary Fig. 13). pDox and free Dox again offered limited survival benefit compared to controls, with Doxil treatment extending median survival by 19 days. However, little to no traces of metastatic tumor-associated bioluminescence was detected in mice treated with iNPG-pDox 4 weeks after treatment, and approximately 40% of mice survived for over 180 days.

MDA-MB-231/MDR cells overexpressing the drug efflux protein P-gp (Fig. 3c) were used to evaluate the ability of the iNPG-pDox particles to overcome multidrug resistance. Cells indeed showed resistance to free Dox (Fig. 3c), as drug efflux proteins on cytoplasmic membranes were capable of sequestering and expelling drug from the cytosol<sup>21</sup>. By contrast, pDox nanoparticles effectively killed MDA-MB-231/MDR cells to a similar degree as parental MDA-MB-231 cells (Supplementary Fig. 4a). In mice bearing lung metastatic MDA-MB-231/MDR tumors, no inhibition of tumor growth was observed from Dox treatment as compared to the PBS control. Contrastingly, iNPG-pDox treatment inhibited tumor growth substantially (Fig. 3d).

Potential toxicity from iNPG-pDox was evaluated in tumor-free athymic nude mice and BALB/c mice, with toxicity compared to those observed following Doxil administration. Whereas both mouse strains survived treatment at 24 mg/kg of iNPG-pDox (4× therapeutic dosage) used in this study, mice were unable to tolerate a dose of 24 mg/kg of Doxil (Supplementary Fig. 14). Moreover, Doxil treatment dramatically reduced total white blood counts at 12 mg/kg and triggered a surge in plasma LDH level, indicating severe cardiac damage. By comparison, iNPG-pDox displayed a mild toxicity profile even at the highest dosage level (Supplementary Fig. 14), indicating a desirable toxicity profile of iNPG-pDox over Doxil.

By partitioning biological barriers encountered by cancer therapeutics *en route* to tumors into distinct tasks, we have developed a multifunctional construct capable of successively overcoming these obstacles. We have demonstrated natural tropism of therapeutic carriers to lungs and liver, preferential organs of metastasis, through rational design with regards to carrier size and geometry. Once localized, high concentrations of Dox were maintained in

these organs for over 1 week after administration, with the particles effectively serving as long-term nanotherapeutic-generating vascular depots.

The pDox molecules were shown to self-assemble *in situ* into nanoparticles, which could in turn extravasate into the tumor interstitium through leaky vasculature<sup>22, 23</sup>, or alternatively through transcytosis. pDox nanoparticles were then internalized into tumor cells via endocytotic pathways, followed by vesicular transport to the perinuclear region and pH-sensitive cleavage of Dox from pDox. This enabled for release of Dox far from the sequestering effects of efflux pumps (e.g. P-glycoprotein) and overcoming of cell membrane-based multidrug resistance mechanisms (Supplementary Fig. 15).

Notably, individual components of this construct did not yield the degree of efficacy observed with the complete particles mainly because deconstructing iNPG-pDox into its individual components, including iNPG, pDox nanoparticles, and Dox, negated proper negotiation of barriers (Fig. 3e). This dramatically reduced its therapeutic impact while significantly increasing adverse side effects. To highlight this, we compared the efficacy of iNPG-pDox to clinical formulations of doxorubicin in two metastatic triple-negative breast cancer mouse models. Triple-negative breast cancer is a subset of the disease that is especially sensitive to anthracycline therapy due to its high proliferative rate, and for which there is currently no targeted therapy. However, in the clinic non-specific distribution hinders efficacy, increases cardiotoxicity, results in multidrug resistance, and eventually, cessation of therapy<sup>24</sup>.

We have developed an approach that has the potential to improve upon these shortcomings by providing a rational material design approach necessary for transport through distinct biological barriers. To the best of our knowledge, no other multicomponent material with the capability of *in situ* generation of nanotherapeutics for sustained site-specific release, acting as intravascular drug depots for prolonged drug exposure at therapeutically relevant concentrations, has been reported before. Although the dimensions and the geometry of silicon particles make the strategy best suited for targeting specific anatomical locations that include the lung and liver, which in turn are major sites of metastasis, the versatility of the silicon-based carrier allows for incorporation of moieties for targeting other organs as well. In principle, the strategy is not limited to one single agent such as Dox, or a specific biomaterial for that matter. Rather, distinct biomaterials may be used as constituent materials of microparticles that encase different drugs and/or multiple drug combinations for therapeutic applications in a variety of disease states.

## Online Methods

### Synthesis and characterization of pDox

Hydrazide groups were conjugated to glutamic acid side chains of poly(L-glutamic acid) via an acid anhydride reaction. Briefly, N-morphylmorline (Sigma-Aldrich) was added to poly(L-glutamic acid) (Sigma-Aldrich) in anhydrous dimethylformamide (DMF), followed by drop-wise addition of isobutyl chloroformate at 4°C under Argon gas. After stirring for 15 min, carbazic acid tert-butyl ester (Sigma-Aldrich) in DMF was added. The resulting solution was allowed to react for 30 min at 4°C followed by 2 h at 25°C. To synthesize the



final product, 100 mg poly(L-glutamic acid hydrazide)-*co*-poly(L-glutamic acid) was dissolved in 200 mL anhydrous methanol, and 100  $\mu$ L of trifluoro acetic acid was added. Dox hydrochloride was then added, and the mixture was stirred at 25°C for 48 h under Argon gas. Polymer Dox was concentrated, dialyzed in methanol, and purified with Sephadex-LH20 (Amersham Pharmacia Biotech Co.).

Gel permeation chromatography (GPC) was carried out to measure molecular weight and polydispersity index of pDox using a Viscotek GPCmax (Houston, TX) equipped with a 7.8 mm  $\times$  30 cm I-MBHMW column (Viscotek, Houston). DMF containing 10 mM LiCl was used as the mobile phase (flow rate, 1.0 mL/min). The GPC system was equipped with a Viscotek TDA 305, a triple detector array including a differential refractive index, a differential viscometer, and a right angle laser light scattering detector. A PEG standard was used for calibration of the GPC apparatus. Molecular weight and distribution were calculated using Viscotek TriSEC GPC. Absence of free Dox was confirmed by GPC. Percentage of Dox in pDox was measured by UV absorbance.

### **Fabrication and characterization of iNPG-pDox**

Discoidal silicon microparticles were fabricated as previously described<sup>25</sup>. Particles were then modified with 2% (v/v) 3-aminopropyltriethoxysilane (APTES) in isopropanol for 48 h at 55°C to conjugate primary amines on the particle surface. iNPG-pDox was assembled by loading concentrated pDox molecules (>10 mg/mL in methanol) into the APTES-modified porous silicon particles followed by vacuum dry. The loading process was repeated to completely fill the nanopores with pDox. To monitor pDox nanoparticle release *in vitro*, iNPG-pDox was incubated in acidic or neutral buffers (pH 5.2, 6.6, 7.4) overnight, and released pDox nanoparticles in the supernatant were collected by centrifugation. Particles sizes were measured with a Multimode 8 AFM system (Bruker Nano). Briefly, a 10  $\mu$ L droplet of released pDox was applied to a freshly-cleaved mica. After incubating for 30 min, the substrate was rinsed with water, and left to air dry. Images were acquired using a ScanAsyst-Air probe with spring constant of 0.4 N/m and 1 Hz scan rate, and were analyzed with the Nanoscope Analysis software (Bruker Nano).

For quantification of Dox release, iNPG-pDox was incubated in acidic or neutral buffers (pH 5.2, 7.4) with 10% FBS. Aliquots were collected at different timepoints, and Dox in solution measured by UV absorbance. Aforementioned GPC was used to measure cleavage of Dox from the prodrug. Briefly, pDox was incubated in PBS (pH 7.4) or phosphate buffer (pH 5.2) overnight and the solution applied to a gel permeation column, and eluted with PBS.

### **Dynamic light scattering (DLS) measurement of particle size distribution**

DLS was applied to measure size distribution of released pDox nanoparticles. Briefly, 1 billion iNPG-pDox particles were suspended in 200  $\mu$ L of PBS (pH 7.4 or 6.6), followed by shaking at 300 rpm in a thermomixer (Eppendorf, Germany) at 37°C for 12 h. Supernatants containing released pDox nanoparticles were collected by centrifugation at 2,000 rpm for 4 min. iNPG controls were prepared by the same procedure with 1 billion empty iNPG particles. pDox NP controls were prepared by direct dispersion of 5  $\mu$ L pDox DMF solution into 2 mL PBS (pH 7.4 or 6.6). Particle size was measured with a Zetasizer Nano-ZS

(Malvern Instruments Ltd, Worcestershire, UK) with measurements made using intensity average.

### **Cryo-TEM examination of released pDox NP**

Released pDox (5  $\mu$ l) was deposited onto freshly glow-discharged holey carbon grids for 1 minute. The grids were blotted with What man filter paper and rapidly vitrified in liquid ethane using a gravity-driven plunger apparatus. The resulting frozen-hydrated specimens were imaged at  $-170^{\circ}\text{C}$  using a Polara G2 electron microscope (FEI Company) equipped with a Field Emission Gun and a Direct Detection Camera (Gatan K2 Summit). The microscope was operated at an accelerating voltage of 300 kV with a magnification of 9,400 $\times$ , resulting the effective pixel size of 4.45  $\text{\AA}$ . For each area of interest, low dose cryo-EM images at  $\sim 5$  defocus were recorded on the Direct Detection Camera. The cumulative doses of  $\sim 30$  e-/A $^2$  were distributed over 30 frames which were subsequently aligned with each other to generate the final high-resolution cryo-EM image.

### **In vitro analysis of iNPG-pDox growth inhibition and intracellular trafficking**

To assess cancer cell killing, cells were seeded into 96-well plates at a seeding density of 5,000 cells/well, and treated with empty iNPG, free Dox, pDox NP, or iNPG- pDox for 96 h. Cell growth and viability was evaluated by incubating with CellTiter Aqueous one solution cell proliferation assay reagent (Promega). Absorbance from each well was measured at 570 nm with a Synergy H4 hybrid reader (BioTek). IC $_{50}$  values were determined with the Graphpad PRISM version 5 software.

To test blockade of pDox nanoparticle uptake by tumor cells, MDA-MB-231 cells were treated for 30 minutes with 20  $\mu\text{M}$  cytochalasin D, 20  $\mu\text{M}$  amiloride, 20  $\mu\text{M}$  dynasore, 120  $\mu\text{M}$  chlorpromazine, or 200  $\mu\text{M}$  genistein. Cells were then incubated with 10  $\mu\text{g/mL}$  pDox for 2 hours. pDox-positive cells were detected by flow cytometry.

To study intracellular pDox trafficking and Dox accumulation, MDA-MB-231 cells were seeded at 1,000 cells/chamber on culture slides (BD Falcon) in DMEM containing 10% FBS. Dox or pDox was added 24 h later, and cells were harvested at different timepoints. To stain late endosomes/lysosomes, cells were incubated with 75 nM LysoTracker Green (Invitrogen) in DMEM for 45 minutes, rinsed with PBS, and fixed with 2.5% formaldehyde for 10 minutes at RT. Slides were mounted with ProLong $^{\circ}$  Gold antifade reagent containing DAPI (Invitrogen). Fluorescent images were captured using a confocal microscope (Nikon A1 Confocal Imaging system).

### **Analysis of tissue distribution of Dox and iNPG-pDox**

Quantification of doxorubicin was performed using daunorubicin (Dau, Sigma) as an internal standard<sup>26</sup>. Briefly, tissues were homogenized in PBS (100 mg tissue/330 mL PBS), and then mixed with 10  $\mu\text{L}$  Dau (50  $\mu\text{g/mL}$ ). A 4-fold volume of the extraction solution containing chloroform and methanol (3/1, v/v) was subsequently added. The mixture was vortexed for 10 minute, and centrifuged at 13,000 rpm for 10 minutes to separate the aqueous and organic phases. The organic phase was collected, and the solvent was vacuum



dried. The extract was dissolved in 200  $\mu$ L methanol, and a 100  $\mu$ L aliquot was used for HPLC analysis.

### Animal studies

All animal studies were performed in accordance with the guidelines of the Animal Welfare Act and the Guide for the Care and Use of Laboratory Animals, following protocols approved by the Institutional Animal Care and Use Committee (IACUC) at the Houston Methodist Research Institute. Murine metastatic models of MDA-MB-231 or MDA-MB-231/MDR tumor cells, transfected with a plasmid carrying both luciferase and GFP genes, were established in nude mice by tail vein inoculation of  $3 \times 10^5$  tumor cells. All mice developed tumor metastases to the lungs, and tumor growth in the lung was visualized by bioluminescence with a Xenogen IVIS-200 system. Experiments to determine the biodistribution and efficacy of iNPG-pDox were carried out in tumor-free athymic nude mice and in murine model of lung metastatic MDA-MB-231 triple negative breast cancer model<sup>27–29</sup>, and were determined by measuring disassembled Dox in blood and major organs 1 h, 1 d, and 7 d post *i.v.* or *i.p.* administration of iNPG-pDox by HPLC, with free Dox and pDox serving as controls. Biodistribution of iNPG-pDox by silicon content was analyzed as previously described<sup>16</sup>. Briefly, animal organs including the heart, liver, spleen, lung, kidney, brain, blood samples were weighed, homogenized in 3 mL of 1N NaOH containing 20% ethanol (v/v), and incubated for 48 h at 20°C. After centrifugation at 4,700 rpm for 30 min, 0.5 mL supernatant was diluted with 2 mL deionized water, and applied to a Varian 720-ES ICP Optical Emission Spectrometer for silicon content measurement.

For examination of iNPG-pDox localization to tumors, mice with metastatic MDA-MB-231 tumor in the lung were treated *i.v.* with 6 mg/kg pDox or iNPG-pDox. Intravital microscopic imaging was performed at 1 h and 24 h timepoints as previously described<sup>17</sup>. Briefly, mice were sacrificed, and the chest cavity immediately opened to expose lungs to imaging. Three mice were imaged per time point. The lung tissues were then processed for histological analysis and for transmission electron microscopy following previously published methods<sup>30</sup>.

Flow cytometry was applied to determine cell types associated with iNPG-pDox and pDox particles. Briefly, mice with advanced stage MDA-MB-231 tumor metastasis were treated, tumor-bearing lungs collected, and tissue samples digested with collagenase to isolate single cells followed by flow cytometry analysis, as described above. For efficacy examination, mice were divided into 6 treatment groups ( $n = 10$  mice/group) and treated weekly with 3 mg/kg Dox, or biweekly with 6 mg/kg Doxil, pDox NP, or iNPG-pDox for 6 weeks. Mice were maintained after treatments until one of the endpoints was met (loss of 10% body weight, fatigue, lethargy, or death).

The orthotopic murine 4T1 tumor model served as the animal model for lung and liver metastases. The 4T1 tumor cells were engineered with luciferase expression for tracking of tumor metastasis by bioluminescence. To initiate lung metastasis, BALB/c mice were inoculated with 4T1 cells ( $3 \times 10^4$ ) into the fourth mammary gland fat pad. Primary tumors were surgically removed once they reached 250 mm<sup>3</sup>. Mice were then treated with negative controls (PBS and iNPG), or with 6 mg/kg Dox, Doxil, pDox NP, and iNPG-pDox weekly

for 4 weeks, and maintained to assess survival benefit. For histological analysis, mice were euthanized at the end of the treatments, and tumor nodules in the lungs were analyzed by H&E staining for growth morphology and Ki-67 staining for cell proliferation.

For examination of resistance *in vivo*, nude mice were inoculated with MDA-MB-231/MDR cells engineered with luciferase expression, and were treated with PBS controls, free Dox or iNPG-pDox. Tumor growth in the lung was monitored weekly by bioluminescence intensity.

### Statistical Analysis

Statistical analyses were performed with the GraphPad Prism 5 (GraphPad Software, Inc., CA, USA) and SAS 9.4 (SAS institute Inc., NC, USA) softwares. For all *in vivo* analysis, sample sizes were chosen to ensure adequate power to detect a pre-specified effect size. Animals were excluded from analysis based on the absence of tumor growth and these criteria were pre-established. Animals were randomized prior to treatment. Blinding was not performed. Differences were evaluated by F-tests of the fixed effects of a two-way ANOVA model and drill down using F-tests of partitions and contrasts of the interaction term. The two-way ANOVA models allowed for the heterogeneous nature of the data and included a random subject effect to account for the data's correlation structure. Hommel's adjustment was applied for multiple comparisons to correct for multiplicity. Survival was estimated by the Kaplan-Meier method and differences in survival were evaluated using log-rank tests. To establish the validity of a linear models approach, the assumption of normality was assessed objectively using a Shapiro-Wilk test and visually by inspecting the normal probability Q-Q plots within each treatment by time period. When necessary, log-transformations were employed to rescale and normalize the data. Global tests were done to establish that significant differences exist, and then pairwise group comparisons were made and adjusted for multiplicity using Hommel's approach. P-values of less than 0.05 and 0.01 were considered statistically significant and very significant, respectively. Data are presented as means  $\pm$  SD or SEM.

### Supplementary Material

Refer to Web version on PubMed Central for supplementary material.

### Acknowledgments

M.F. is grateful for the Ernest Cockrell Jr. Distinguished Endowed Chair in the Department of Nanomedicine at the Houston Methodist Research Institute. The authors acknowledge financial support from Department of Defense grants W81XWH-09-1-0212 and W81XWH-12-1-0414, National Institute of Health grants NIH U54CA143837, U54CA151668 (M.F.) and 1R01CA193880-01A1 (H.S.), Welch Foundation grant AU-1714 (J.L.), and National Natural Science Foundation of China 81301314 (R.X.). The authors thank the Nanofabrication Core of the Houston Methodist Research Institute for porous silicon microparticle fabrication and surface chemical modification. Dr. Jianhua Gu is acknowledged for AFM analysis, Dr. Dickson Kirui for intravital microscopy, and Dr. Hanh H. Hoang for manuscript proof-reading and editing.

### References

1. Blanco E, Shen H, Ferrari M. Principles of nanoparticle design for overcoming biological barriers to drug delivery. *Nat Biotechnol.* 2015; 33:941–951. [PubMed: 26348965]

2. Ferrari M. Frontiers in cancer nanomedicine: directing mass transport through biological barriers. *Trends Biotechnol.* 2010; 28:181–188. [PubMed: 20079548]
3. Michor F, Liphardt J, Ferrari M, Widom J. What does physics have to do with cancer? *Nat Rev Cancer.* 2011; 11:657–670. [PubMed: 21850037]
4. Lien MY, et al. Safety and efficacy of pegylated liposomal doxorubicin-based adjuvant chemotherapy in patients with stage I–III triple-negative breast cancer. *Anticancer Res.* 2014; 34:7319–7326. [PubMed: 25503167]
5. Verma S, Dent S, Chow BJ, Rayson D, Safra T. Metastatic breast cancer: the role of pegylated liposomal doxorubicin after conventional anthracyclines. *Cancer Treat Rev.* 2008; 34:391–406. [PubMed: 18358614]
6. Patel HM, Moghimi SM. Serum-mediated recognition of liposomes by phagocytic cells of the reticuloendothelial system - The concept of tissue specificity. *Adv Drug Deliv Rev.* 1998; 32:45–60. [PubMed: 10837635]
7. Decuzzi P, et al. Size and shape effects in the biodistribution of intravascularly injected particles. *J Control Release.* 2010; 141:320–327. [PubMed: 19874859]
8. Lesniak A, et al. Nanoparticle adhesion to the cell membrane and its effect on nanoparticle uptake efficiency. *J Am Chem Soc.* 2013; 135:1438–1444. [PubMed: 23301582]
9. Gottesman MM, Fojo T, Bates SE. Multidrug resistance in cancer: role of ATP-dependent transporters. *Nat Rev Cancer.* 2002; 2:48–58. [PubMed: 11902585]
10. Peer D, et al. Nanocarriers as an emerging platform for cancer therapy. *Nat Nanotechnol.* 2007; 2:751–760. [PubMed: 18654426]
11. Tasciotti E, et al. Mesoporous silicon particles as a multistage delivery system for imaging and therapeutic applications. *Nat Nanotechnol.* 2008; 3:151–157. [PubMed: 18654487]
12. Bae Y, Fukushima S, Harada A, Kataoka K. Design of environment-sensitive supramolecular assemblies for intracellular drug delivery: polymeric micelles that are responsive to intracellular pH change. *Angew Chem Int Ed Engl.* 2003; 42:4640–4643. [PubMed: 14533151]
13. Demaurex N. pH Homeostasis of cellular organelles. *News Physiol Sci.* 2002; 17:1–5. [PubMed: 11821527]
14. Padilla-Parra S, et al. Quantitative imaging of endosome acidification and single retrovirus fusion with distinct pools of early endosomes. *Proc Natl Acad Sci U S A.* 2012; 109:17627–17632. [PubMed: 23047692]
15. Decuzzi P, Pasqualini R, Arap W, Ferrari M. Intravascular delivery of particulate systems: does geometry really matter? *Pharm Res.* 2009; 26:235–243. [PubMed: 18712584]
16. Godin B, et al. Discoidal Porous Silicon Particles: Fabrication and Biodistribution in Breast Cancer Bearing Mice. *Adv Funct Mater.* 2012; 22:4225–4235. [PubMed: 23227000]
17. van de Ven AL, et al. Rapid tumortropic accumulation of systemically injected plateloid particles and their biodistribution. *J Control Release.* 2012; 158:148–155. [PubMed: 22062689]
18. Wike-Hooley JL, Haveman J, Reinhold HS. The relevance of tumour pH to the treatment of malignant disease. *Radiother Oncol.* 1984; 2:343–366. [PubMed: 6097949]
19. Von Hoff DD, et al. Risk factors for doxorubicin-induced congestive heart failure. *Ann Intern Med.* 1979; 91:710–717. [PubMed: 496103]
20. Zhang S, et al. Identification of the molecular basis of doxorubicin-induced cardiotoxicity. *Nat Med.* 2012; 18:1639–1642. [PubMed: 23104132]
21. Fojo T, Menefee M. Mechanisms of multidrug resistance: the potential role of microtubule-stabilizing agents. *Ann Oncol.* 2007; 18(Suppl 5):v3–v8. [PubMed: 17656560]
22. Maeda H. The enhanced permeability and retention (EPR) effect in tumor vasculature: the key role of tumor-selective macromolecular drug targeting. *Adv Enzyme Regul.* 2001; 41:189–207. [PubMed: 11384745]
23. Maeda H. Toward a full understanding of the EPR effect in primary and metastatic tumors as well as issues related to its heterogeneity. *Adv Drug Deliv Rev.* 2015; 91:3–6. [PubMed: 25579058]
24. Liedtke C, et al. Response to neoadjuvant therapy and long-term survival in patients with triple-negative breast cancer. *J Clin Oncol.* 2008; 26:1275–1281. [PubMed: 18250347]

## References

25. Shen H, et al. Cooperative, nanoparticle-enabled thermal therapy of breast cancer. *Adv Healthc Mater.* 2012; 1:84–89. [PubMed: 23184690]
26. Alhareth K, Vauthier C, Gueutin C, Ponchel G, Moussa F. HPLC quantification of doxorubicin in plasma and tissues of rats treated with doxorubicin loaded poly(alkylcyanoacrylate) nanoparticles. *J Chromatogr B Analyt Technol Biomed Life Sci.* 2012; 887–888:128–132.
27. Hurst DR, et al. Breast cancer metastasis suppressor 1 up-regulates miR-146, which suppresses breast cancer metastasis. *Cancer Res.* 2009; 69:1279–1283. [PubMed: 19190326]
28. Lu X, Kang Y. Efficient acquisition of dual metastasis organotropism to bone and lung through stable spontaneous fusion between MDA-MB-231 variants. *Proc Natl Acad Sci U S A.* 2009; 106:9385–9390. [PubMed: 19458257]
29. Minn AJ, et al. Genes that mediate breast cancer metastasis to lung. *Nature.* 2005; 436:518–524. [PubMed: 16049480]
30. McConnell KI, et al. Enhanced gene delivery in porcine vasculature tissue following incorporation of adeno-associated virus nanoparticles into porous silicon microparticles. *J Control Release.* 2014; 194:113–121. [PubMed: 25180449]

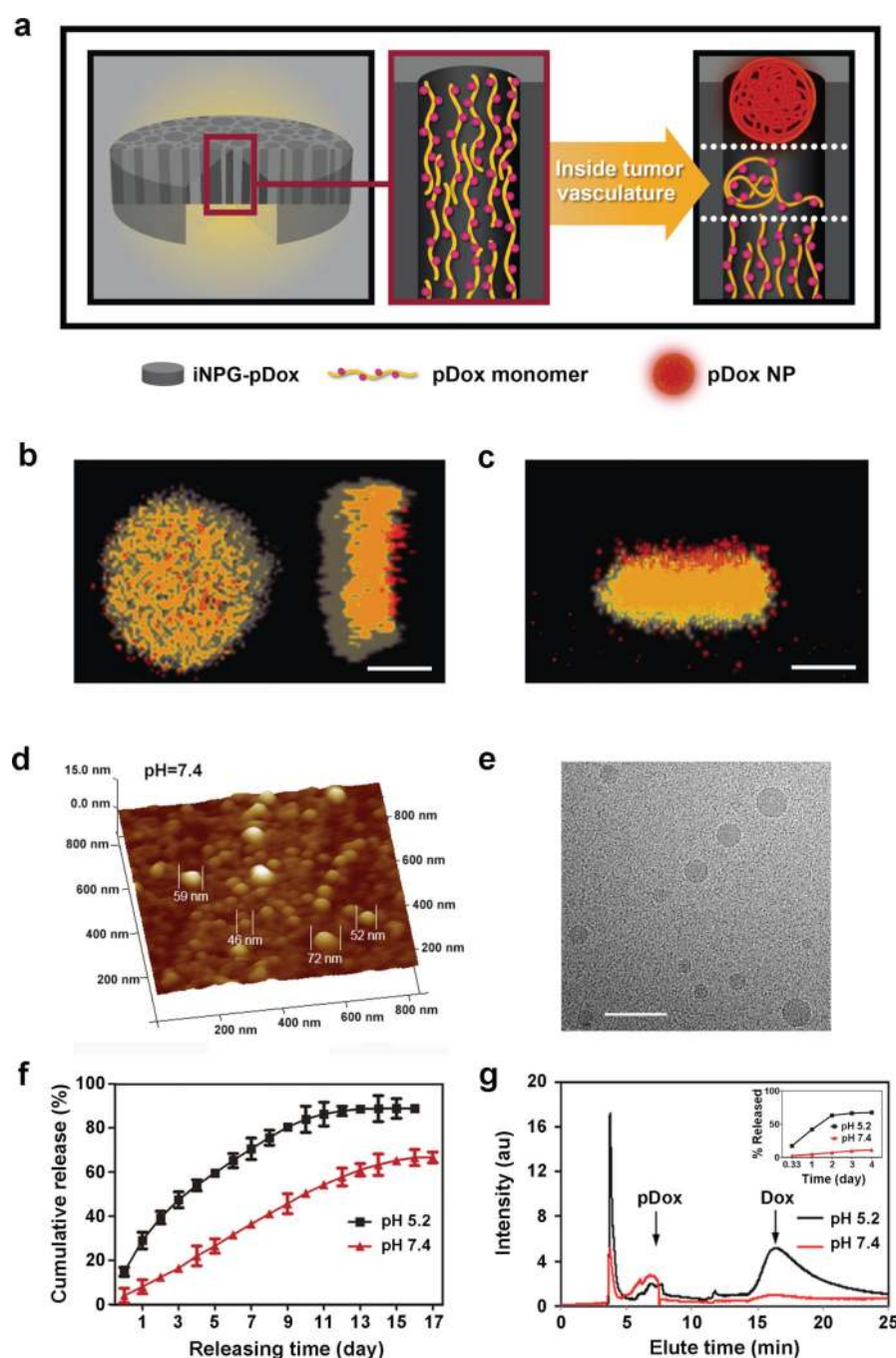


**Figure 1. iNPG-pDox characterization and pDox assembly and release from iNPG**  
 (a) Schematic diagram depicting iNPG-pDox composition, pDox prodrug encapsulation, and pDox nanoparticle assembly and release from nanopores. (b) Z-series confocal microscopy imaging of the iNPG-pDox particles, highlighting the presence of pDox (red) within the nanopores of the silicon carrier particle (gray). Scale bar: 1  $\mu$ m. (c) Three dimensional reconstruction following sagittal cross-sectioning of the iNPG-pDox particles, depicting pDox (red) within the nanopores of the silicon carrier particle (gray), as well as the presence of pDox nanoparticles (red) released from the microparticles. Scale bar: 1  $\mu$ m. (d) AFM

analysis of size distribution of pDox nanoparticles released from iNPG-pDox at pH 7.4. (e) Cryogenic TEM of pDox nanoparticles released from iNPG-pDox at pH 7.4. Scale bar: 150 nm. (f) Release of pDox or disassembled Dox from iNPG-pDox at pH 7.4 and pH 5.2 in 10% FBS. (g) Gel permeation chromatography (GPC) analysis on released pDox and disseminated Dox from iNPG-pDox. pDox was the predominant form at pH 7.4, whereas Dox was released from the polymer at pH 5.2. The inset represents release of Dox in different pH conditions following cleavage from pDox.



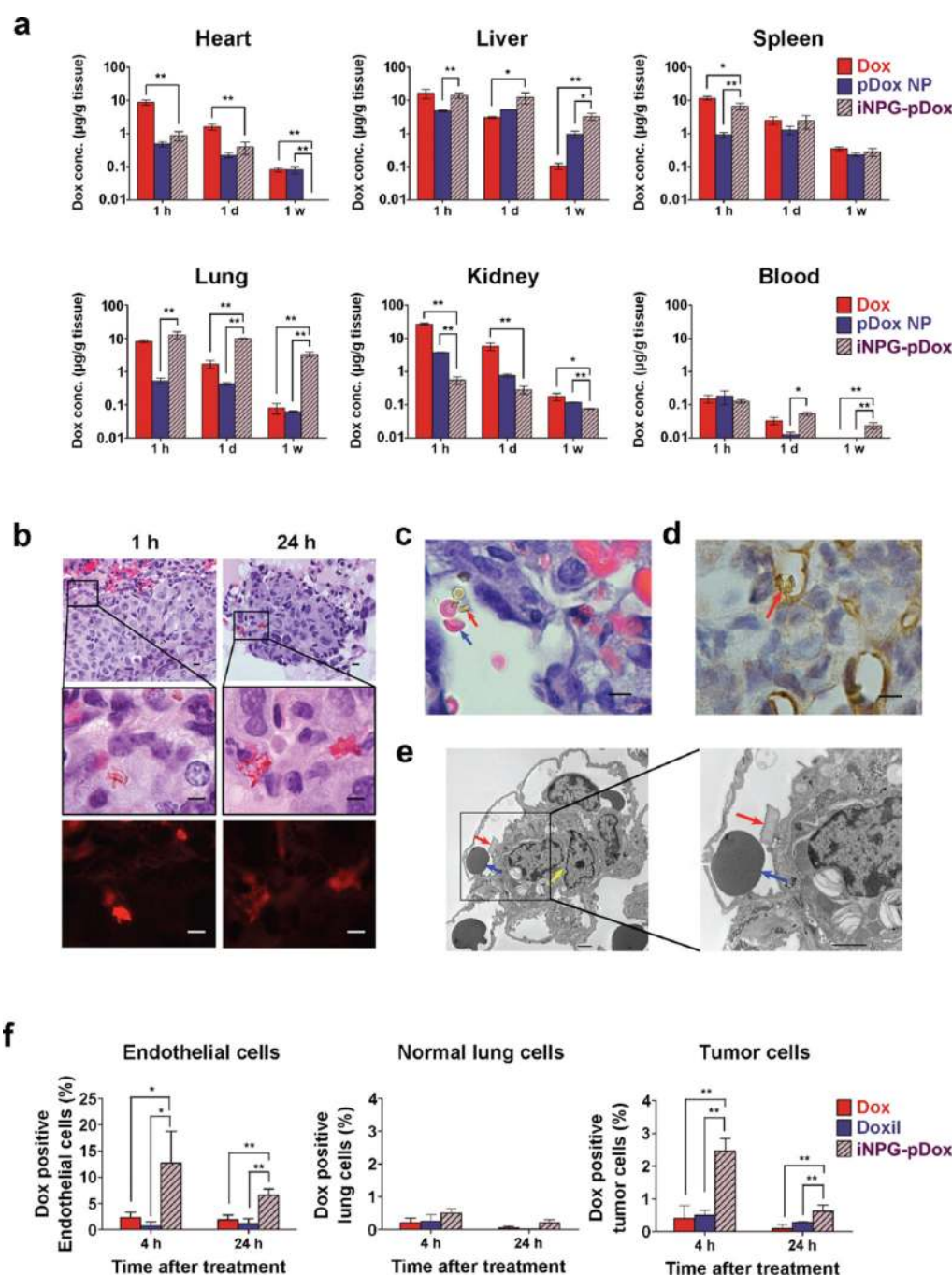


**Figure 2. Accumulation of iNPG-pDox in metastatic MDA-MB-231 tumors**

(a) Time-dependent tissue biodistribution based on Dox content in mice with MDA-MB-231 lung metastasis after administration of 6 mg/kg Dox, pDox NP, or iNPG-pDox. Differences and significance between iNPG-pDox and Dox or pDox NP were estimated by F-tests with Hommel's adjustment of multiplicity. (b) iNPG-pDox accumulation in lung metastatic tumors by H&E staining (upper and middle panels). Presence of doxorubicin inside iNPG was visualized under fluorescence microscopy (bottom panel). Scale bar: 10  $\mu$ m. (c) H&E histological evaluation of tumor nodules, demonstrating co-localization of iNPG-pDox with

red blood cells and attachment on tumor microvessels. The red arrow points to an iNPG particle, and blue arrow points to red blood cells. The scale bar represents 5  $\mu\text{m}$ . (d) CD31 staining for tumor microvessels (brown). The red arrow points to an iNPG particles. The scale bar represents 5  $\mu\text{m}$ . (e) TEM analysis of iNPG attachment to microvessel walls in tumor-bearing lung tissues collected 24 h after iNPG-pDox treatment. The red arrow points to an iNPG particle, the yellow arrow points to a tumor cell, and the blue arrow points to a red blood cell inside the vessel. Scale bar: 2  $\mu\text{m}$ . (f) Flow cytometry analysis of Dox distribution in CD31<sup>+</sup> endothelial cells, HLA-ABC<sup>+</sup> tumor cells, and HLA-ABC<sup>-</sup>/CD45<sup>-</sup>/CD31<sup>-</sup> normal lung cells isolated from post-treatment mice. \*:  $p < 0.05$ ; \*\*:  $p < 0.01$

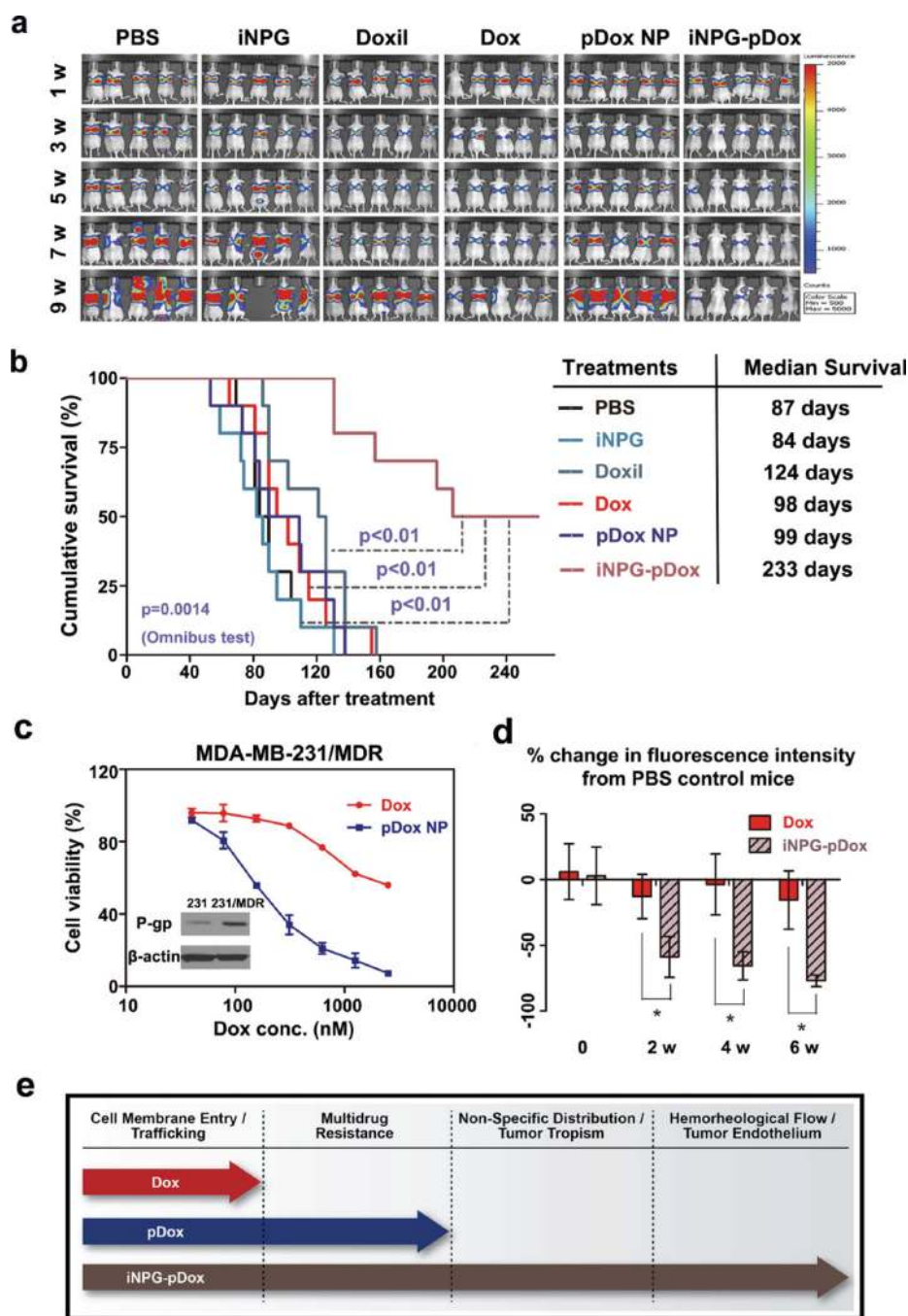


**Figure 3. *In vivo* growth inhibition of lung metastatic MDA-MB-231 tumors, as well as a multidrug resistant cell line, following iNPG-pDox treatment**

(a) Bioluminescence monitoring of MDA-MB-231 tumor metastasis in the lung. Nude mice were inoculated with MDA-MB-231 cells carrying a luciferase gene, divided into 6 treatment groups (n = 10 mice/group), and treated weekly with 3 mg/kg Dox or biweekly with 6 mg/kg Doxil, pDox, or iNPG-pDox for 6 weeks. Mice were maintained further thereafter to monitor survival. Images of 5 mice/group are shown. (b) Kaplan-Meier plot of animal survival with median survival time listed in the table. Differences in survival were evaluated by the log-rank test. A global test demonstrated a difference exists among the

groups. Pairwise comparisons were performed to evaluate the advantage of iNPG-pDox formulation over the clinical formulations. (c) MTT cell viability assay of MDA-MB-231/MDR cells treated with Dox or pDox NP for 72 h. The inset represents Western blot analysis of P-gp expression in the parental MDA-MB-231 cells and cells transfected with a plasmid carrying the *MDR1* gene. (d) Tumor growth in the lung, as measured based on bioluminescence and compared to that of the PBS control group, of mice inoculated with MDA-MB-231/MDR cells carrying a luciferase gene following biweekly administration of PBS, Dox, or iNPG-pDox at a dosage of 6 mg/kg. F-tests of the simple effects were applied to compare the effects of Dox and iNPG-pDox treatments at each time period. (e) Schematic diagram demonstrating the individual components of the iNPG-pDox construct, and the distinct biological barriers that each component is capable of overcoming following systemic administration.